PCCP

ROYAL SOCIETY OF CHEMISTRY

PAPER

View Article Online
View Journal | View Issue

Cite this: *Phys. Chem. Chem. Phys.*, 2024, **26**, 7492

Carbon-coated $Ni_{0.5}Mg_{0.5}Fe_{1.7}Mn_{0.3}O_4$ nanoparticles as a novel anode material for high energy density lithium-ion batteries†

Khadija Kouchi,[a] Marwa Tayoury,[a] Abdelwahed Chari,[a] Loubna Hdidou,[a] Zakaria Chchiyai,[b] Khadija El kamouny,[c] Youssef Tamraoui,[a] Bouchaib Manoun,[ab] Jones Alami[a] and Mouad Dahbi *[a]

Lithium-ion batteries (LIBs) have gained considerable attention from the scientific community due to their outstanding properties, such as high energy density, low self-discharge, and environmental sustainability. Among the prominent candidates for anode materials in next-generation LIBs are the spinel ferrites, represented by the MFe_2O_4 series, which offer exceptional theoretical capacities, excellent reversibility, cost-effectiveness, and eco-friendliness. In the scope of this study, $Ni_{0.5}Mg_{0.5}Fe_{1.7}Mn_{0.3}O_4$ nanoparticles were synthesized using a sol–gel synthesis method and subsequently coated with a carbon layer to further enhance their electrochemical performance. TEM images confirmed the presence of the carbon coating layer on the $Ni_{0.5}Mg_{0.5}Fe_{1.7}Mn_{0.3}O_4$/C composite. The analysis of the measured X-ray diffraction (XRD) and Raman spectroscopy results confirmed the formation of nanocrystalline $Ni_{0.5}Mg_{0.5}Fe_{1.7}Mn_{0.3}O_4$ before coating and amorphous carbon in the $Ni_{0.5}Mg_{0.5}Fe_{1.7}Mn_{0.3}O_4$/C after the coating. The $Ni_{0.5}Mg_{0.5}Fe_{1.7}Mn_{0.3}O_4$ anode material exhibited a much higher specific capacity than the traditional graphite material, with initial discharge/charge capacities of 1275 and 874 mA h g^{-1}, respectively, at a 100 mA g^{-1} current density and a first coulombic efficiency of 68.54%. The long-term cycling test showed a slight capacity fading, retaining approximately 85% of its initial capacity after 75 cycles. Notably, the carbon-coating layer greatly enhanced the stability and slightly increased the capacity of the as-prepared $Ni_{0.5}Mg_{0.5}Fe_{1.7}Mn_{0.3}O_4$. The first discharge/charge capacities of $Ni_{0.5}Mg_{0.5}Fe_{1.7}Mn_{0.3}O_4$/C at 100 mA g^{-1} current density reached 1032 and 723 mA h g^{-1}, respectively, and a first coulombic efficiency of 70.06%, with an increase of discharge/charge capacities to 826.6 and 806.2 mA h g^{-1}, respectively, after 75 cycles (with a capacity retention of 89.7%), and a high-rate capability of 372 mA h g^{-1} at 2C. Additionally, a full cell was designed using a $Ni_{0.5}Mg_{0.5}Fe_{1.7}Mn_{0.3}O_4$/C anode and an NMC811 cathode. The output voltage was about 2.8 V, with a high initial specific capacity of 755 mA h g^{-1} at 0.125C, a high rate-capability of 448 mA h g^{-1} at 2C, and a high-capacity retention of 91% after 30 cycles at 2C. The carbon coating layer on $Ni_{0.5}Mg_{0.5}Fe_{1.7}Mn_{0.3}O_4$ nanoparticles played a crucial role in the excellent electrochemical performance, providing conducting, buffering, and protective effects.

Received 15th January 2024,
Accepted 22nd January 2024

DOI: 10.1039/d4cp00182f

rsc.li/pccp

1. Introduction

Lithium-ion batteries (LIBs) have shown great promise as an energy storage solution, finding extensive use across various domains encompassing portable devices, electric vehicles, and grid-scale energy systems.[1] Their exceptional attributes, such as high energy density and prolonged cycle life, make them particularly appealing.[2] LIBs consist of crucial constituents, namely the cathode, anode, electrolyte, and separator. Their effectiveness is contingent on the chemical composition of their diverse constituents and the morphology of their electrode materials.[3] Hence, there is a need to develop new efficient

[a] *Materials Science, Energy, and Nano-engineering Department, Mohammed VI Polytechnic University, Lot 660-Hay Moulay Rachid, 43150, Ben Guerir, Morocco. E-mail: Mouad.dahbi@um6p.ma*
[b] *Hassan First University, FST Settat, Rayonnement-Matière et Instrumentation, S3M, 26000, Settat, Morocco*
[c] *Green Tech Institute Department, Mohammed VI Polytechnic University UM6P, Ben Guerir, Morocco*

† Electronic supplementary information (ESI) available. See DOI: https://doi.org/10.1039/d4cp00182f

and cost-effective electrode materials to meet the growing demand for renewable energy, portable electronic devices, electric transportation, and large-scale energy storage in smart grids.[4,5] Due to its cost-effectiveness, reliable reversibility concerning lithium-ion insertion/extraction, and plentiful availability, graphite is extensively utilized as the active anode material in commercial lithium-ion batteries (LIBs). Nevertheless, graphite is hindered by its low theoretical capacity of merely 372 mA h g^{-1}, which falls short of meeting the demands of extensive utilization in the green energy storage network.[6–8] Furthermore, the utilization of graphite in battery systems gives rise to safety considerations owing to its relatively low working voltage, which is less than 0.2 V when compared to the Li/Li^+ standard, and this can lead to the formation of lithium dendrites.[9,10] Silicon-based materials have emerged as a promising alternative to graphite for battery systems due to their large capacities. However, significant volume changes during the lithiation–delithiation process present a major obstacle to their practical application.[11]

To overcome the shortcomings associated with graphite and silicon-based anodes, spinel $Li_4Ti_5O_{12}$ is another anode material that has been used for LIBs. Its discharge potential is about 1.5 V, which makes it safer than the commonly used graphite anode because the problem of lithium plating can be largely avoided.[12] The $Li_4Ti_5O_{12}$ demonstrates outstanding stability and specific capacity at high current densities. However, its theoretical capacity is limited to 175 mA h g^{-1}.[13] As a result, more research is necessary to develop new anode materials that offer improved safety, low cost, high theoretical capacity, and easy synthesis processes.

Spinel ferrite oxides, including $ZnFe_2O_4$,[14] $CoFe_2O_4$,[15] $NiFe_2O_4$,[16] $CuFe_2O_4$,[17] $MgFe_2O_4$,[18] *etc.*, have gained considerable interest as potential anode materials for use in lithium-ion batteries (LIBs). This is largely because they have significantly higher theoretical capacities compared to graphite and $Li_4Ti_5O_{12}$ anode materials.[19,20]

For instance, $CaFe_2O_4$, $CoFe_2O_4$, $NiFe_2O_4$, and $CuFe_2O_4$ exhibited higher specific capacities than the traditional graphite (372 mA h g^{-1}). $ZnFe_2O_4$ can also be considered as a good anode material candidate owing to its elevated theoretical specific capacity of around 1000 mA h g^{-1}.[21]

However, the main problems of spinel oxide anode materials are their low electrical conductivity and considerable volume expansion.[22] To overcome these issues, carbon coating has been reported as a suitable coating material that can effectively enhance the capacity retention and cycling stability of spinel materials.[17] Moreover, it participates in reducing the volume change during the discharging/charging operations and facilitates the Li-ion diffusion into the metal oxide structure.[13]

For example, Jin *et al.* have successfully prepared $CuFe_2O_4$/C hollow spheres through a hydrothermal growth method based on polymers, followed by calcination. After the 70th cycle at a current density of 100 mA cm^{-2}, the anodic material demonstrated a specific capacity of 550 mA h g^{-1}, which is significantly greater than the initial specific capacity of the $CuFe_2O_4$ hollow spheres ($\sim$120 mA h g^{-1}).[23] In addition, Deng *et al.* reported a significant enhancement in the electrochemical properties of $ZnFe_2O_4$/C hollow spheres. They found that the $ZnFe_2O_4$ sample modified with carbon exhibited a specific capacity of 841 mA h g^{-1} after 30 cycles, along with a high-rate capability.[24]

To our knowledge, no studies have reported on the electrochemical performances of nanocrystalline $Ni_{0.5}Mg_{0.5}Fe_{1.7}Mn_{0.3}O_4$ as anode materials for LIBs. This study details the preparation of $Ni_{0.5}Mg_{0.5}Fe_{1.7}Mn_{0.3}O_4$ and $Ni_{0.5}Mg_{0.5}Fe_{1.7}Mn_{0.3}O_4$/C nanoparticles, aiming to explore their potential as LIB anodes. We enhanced the cycling stability and rate capability of $Ni_{0.5}Mg_{0.5}Fe_{1.7}Mn_{0.3}O_4$ anode through carbon coating. The nanocrystalline powders were characterized using X-ray diffraction (XRD), scanning electron microscopy (SEM), transmission electron microscopy (TEM), and Raman spectroscopy. The anode materials' performance for LIBs was evaluated using electrochemical tests in a lithium half-cell, including cyclic voltammetry, galvanostatic charge–discharge, and electrochemical impedance spectroscopy (EIS) tests. Additionally, the carbon-coated $Ni_{0.5}Mg_{0.5}Fe_{1.7}Mn_{0.3}O_4$/C anode's performance for LIBs was specifically evaluated in the full-cell configuration.

2. Experimental

2.1. Synthesis of $Ni_{0.5}Mg_{0.5}Fe_{1.7}Mn_{0.3}O_4$ and $Ni_{0.5}Mg_{0.5}Fe_{1.7}Mn_{0.3}O_4$/C samples

The synthesis of the $Ni_{0.5}Mg_{0.5}Fe_{1.7}Mn_{0.3}O_4$ spinel material was conducted utilizing the sol–gel method, as detailed in a prior study.[25] A solution was prepared by dissolving $Ni(NO_3)_2{\cdot}6H_2O$, $Mg(NO_3)_2{\cdot}6H_2O$, $FeCl_3{\cdot}6H_2O$, and $MnCl_2{\cdot}4H_2O$ in distilled water, maintaining a molar ratio of Ni : Mg : Fe : Mn = 0.5 : 0.5 : 1.7 : 0.3. Citric acid, acting as a complexing agent, was subsequently introduced to this mixture. This combined solution was then heated to 90 °C with continuous stirring until it transformed into a viscous gel. The gel underwent a drying process at a temperature of 160 °C for a duration of 12 hours, resulting in the formation of a xerogel. Subsequently, the xerogel underwent calcination in an ambient air environment within a temperature range of 250–800 °C. Prior to each calcination phase, the sample was subjected to intermediate grindings.

In this synthesis process, the reagents reacted to produce the $Ni_{0.5}Mg_{0.5}Fe_{1.7}Mn_{0.3}O_4$ spinel oxide, as depicted by the subsequent chemical equation:

$$0.5\ Ni(NO_3)_2{\cdot}6H_2O + 0.5\ Mg(NO_3)_2{\cdot}6H_2O + 1.7\ FeCl_3{\cdot}6H_2O + 0.3\ MnCl_2{\cdot}4H_2O \rightarrow Ni_{0.5}Mg_{0.5}Fe_{1.7}Mn_{0.3}O_4 + 2.85\ Cl_2\uparrow + 2\ NO_2\uparrow + 17.4\ H_2O\uparrow$$

Carbon coating was performed by mixing the as-synthesized $Ni_{0.5}Mg_{0.5}Fe_{1.7}Mn_{0.3}O_4$ material with sucrose powder as the carbon source ($Ni_{0.5}Mg_{0.5}Fe_{1.7}Mn_{0.3}O_4$: glucose = 95 : 5, which was the percentage) using acetone solution. Subsequently, the composite underwent a calcination process at a temperature of

600 °C for a duration of 5 hours, while being exposed to an argon environment to get the $Ni_{0.5}Mg_{0.5}Fe_{1.7}Mn_{0.3}O_4$/C sample.

2.2. Material characterization

The sample was characterized using X-ray diffraction (XRD) analysis with a "BRUKER D8 ADVANCE" diffractometer, equipped with a Cu Kα radiation source (λ = 1.54056 Å). The diffraction data was collected within the 10 to 100 degrees (2θ) angular range, using a step size of 0.01 degrees and a count time of 10 seconds per step. To investigate the morphology and particle size of the sample, scanning electron microscopy (SEM) was performed using a JEOL JSM-IT500HRL instrument. The chemical compositions of the $Ni_{0.5}Mg_{0.5}Fe_{1.7}Mn_{0.3}O_4$ material were examined using energy-dispersive spectroscopy (EDS). Transmission Electron Microscopy (TEM) using the TECNAI G2/FEI model was used to study the microstructure of both uncoated and carbon-coated samples and to assess the state of the carbon coating layer. Energy dispersive spectroscopy (EDS) was used to analyze the surface composition and elemental content of the carbon-coated $Ni_{0.5}Mg_{0.5}Fe_{1.7}Mn_{0.3}O_4$/C sample. Raman spectroscopy analysis was conducted to identify the vibrational bands present in the $Ni_{0.5}Mg_{0.5}Fe_{1.7}Mn_{0.3}O_4$ sample, and to investigate the presence of carbon in the synthesized $Ni_{0.5}Mg_{0.5}Fe_{1.7}Mn_{0.3}O_4$/C material. This analysis was carried out with a spectrometer (Horiba) and an excitation wavelength of 532 cm^{-1}, using the spectral range of 100–2000 cm^{-1}.

2.3. Electrochemical measurements

The working electrodes for electrochemical tests were prepared by combining 70 wt% of the active material, 20 wt% of carbon black as a conductive agent, and 10 wt% of CarboxyMethyl Cellulose (CMC) as a binder. The resulting mixture was dispersed in double-distilled water and agitated for 6 hours to form a viscous slurry. The doctor-blade technique was employed to uniformly apply the slurry onto a copper foil current collector with a thickness of 0.1 mm, where the mass loading was 1.3–1.5 mg cm^{-2}. The loaded copper foil was then dried overnight at 65 °C to remove the solvent (water). It was cut into disks of 11 mm diameter and left to further dry out overnight in a vacuum oven at 100 °C to eliminate all remaining solvent. The electrochemical tests of the fabricated materials were carried out using CR2032 button cells in a half-cell setup. The half-cells containing uncoated and carbon-coated materials were assembled under controlled conditions within an argon-filled glove box (Jacomex, France) at ambient temperature, while ensuring that water and oxygen levels remained below 0.5 ppm. The electrodes used in the setup comprised of a Li metal disc with an 8 mm diameter serving as the counter and reference electrodes. A Whatman separator was employed to segregate the negative and positive electrodes. The electrolyte adopted was a 2.0 M $LiPF_6$ solution dissolved in ethylene carbonate (EC) and diethyl carbonate (DEC), mixed in a 1 : 1 proportion. Each coin cell contained 120 μL of this electrolyte.

The galvanostatic discharge/charge and long-term cycling tests on the newly investigated uncoated and coated spinel oxide were carried out at a current density of 100 mA g^{-1} (100 mA g^{-1} = 0.125C) over the 0.01–3.00 V voltage range. Rate capability analysis was conducted at various C-rates, including 0.03C, 0.06C, 0.125C, 0.25C, 0.625C, 1.25C and 2C. Cyclic voltammetry curves of uncoated electrode $Ni_{0.5}Mg_{0.5}Fe_{1.7}Mn_{0.3}O_4$ were obtained by varying the potential between 0.01 V and 3.0 V and utilizing a scan rate of 1 mV s^{-1}. Electrochemical impedance spectra (EIS) were characterized over a frequency range of 100 kHz to 0.01 Hz. The electrochemical testing of the full cell was carried out at a current density of 100 mA g^{-1}, within a voltage range of 1–4 V. For this, we used an NMC811 electrode, sourced from Argonne National Laboratory, as the positive electrode, and our synthesized carbon-coated spinel oxide $Ni_{0.5}Mg_{0.5}Fe_{1.7}Mn_{0.3}O_4$/C as the negative electrode. The full cell, comprising NMC811 *vs.* $Ni_{0.5}Mg_{0.5}Fe_{1.7}Mn_{0.3}O_4$/C, was assembled using the same procedure as for the half-cells of $Ni_{0.5}Mg_{0.5}Fe_{1.7}Mn_{0.3}O_4$ and $Ni_{0.5}Mg_{0.5}Fe_{1.7}Mn_{0.3}O_4$/C negative electrodes. However, in the full-cell configuration, the NMC811 electrode was used instead of the lithium metal disc. The N/P (negative/positive) mass ratio was maintained at approximately 0.84. A discharge/charge rate of 0.125C and 2C was applied, corresponding to a specific current of 100 mA g^{-1} and 1600 mA g^{-1} for the negative electrode material. All potentials were referenced to the Li/Li^+ electrode. It should be noted that discharging and charging were regarded as lithiation and delithiation processes in this study. All electrochemical tests were conducted at ambient temperature utilizing a multi-channel potentiostat (MPG-2, Bio-Logic).

3. Results and discussion

The crystal structure of the $Ni_{0.5}Mg_{0.5}Fe_{1.7}Mn_{0.3}O_4$ spinel oxide and the incorporation of carbon were characterized using X-ray diffraction (XRD) and Raman spectroscopy techniques. Fig. 1 displays the X-ray diffraction pattern acquired at ambient temperature for the uncoated $Ni_{0.5}Mg_{0.5}Fe_{1.7}Mn_{0.3}O_4$ powder that underwent thermal treatment at a temperature of 800 °C,

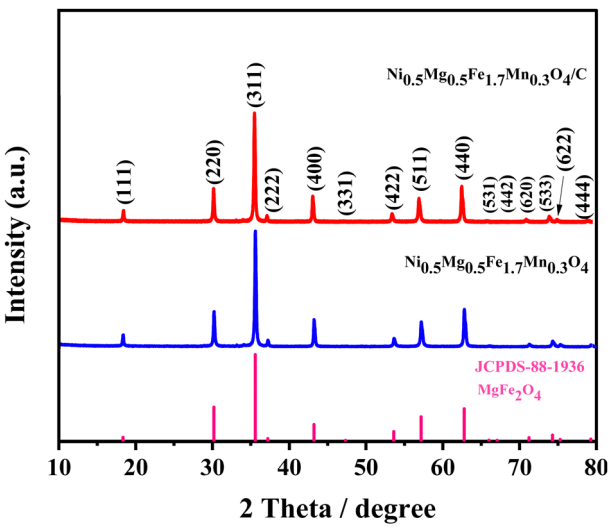

Fig. 1 Room temperature XRD patterns of the synthesized $Ni_{0.5}Mg_{0.5}Fe_{1.7}Mn_{0.3}O_4$ and $Ni_{0.5}Mg_{0.5}Fe_{1.7}Mn_{0.3}O_4$/C materials.

and carbon coated $Ni_{0.5}Mg_{0.5}Fe_{1.7}Mn_{0.3}O_4$/C powder. The X-ray diffraction (XRD) peaks observed in the diffraction pattern of uncoated material $Ni_{0.5}Mg_{0.5}Fe_{1.7}Mn_{0.3}O_4$ have been successfully identified and assigned to the cubic spinel structure with $Fd\bar{3}m$ (no. 227) as the corresponding space group.[26] No additional peaks corresponding to other phases were observed in the X-ray diffraction (XRD) pattern, indicating that the $Ni_{0.5}Mg_{0.5}Fe_{1.7}Mn_{0.3}O_4$ compound synthesized and subjected to thermal treatment at 800 °C is a pure single-phase spinel material. This outcome can be attributed to the chelation of citric acid molecules with the cations (Ni^{2+}, Mg^{2+}, Fe^{3+}, and Mn^{2+}) during the synthesis process, which effectively hinders the formation of impurities. The obtained sample of $Ni_{0.5}Mg_{0.5}Fe_{1.7}Mn_{0.3}O_4$ exhibits a notable level of crystallinity, which is supported by the clear existence of distinct X-ray diffraction (XRD) peaks characterized by narrow full width at half maximum (FWHM) values.[27] The determined crystallite size of the $Ni_{0.5}Mg_{0.5}Fe_{1.7}Mn_{0.3}O_4$ material is 38 nm. The X-ray powder diffraction patterns of the sample $Ni_{0.5}Mg_{0.5}Fe_{1.7}Mn_{0.3}O_4$ were analyzed using High-Score software, as depicted in Fig. 1. The analysis of the $Ni_{0.5}Mg_{0.5}Fe_{1.7}Mn_{0.3}O_4$ combination demonstrated that all the diffraction peaks could be accurately identified as originating from the single-phase cubic spinel $MgFe_2O_4$. The space group $Fd\bar{3}m$ was utilized for indexing, with reference to the standard JCPDS card (no. 88-1936) and a lattice parameter of a = 8.3827 Å. The obtained outcome was compared to the pure $MgFe_2O_4$.[28]

The X-ray diffraction (XRD) pattern of the carbon-coated $Ni_{0.5}Mg_{0.5}Fe_{1.7}Mn_{0.3}O_4$/C composite did not reveal any diffraction peaks for carbon, indicating that the carbon produced from glucose decomposition may be amorphous.[29] In addition, there is no apparent difference between the XRD patterns of uncoated $Ni_{0.5}Mg_{0.5}Fe_{1.7}Mn_{0.3}O_4$ and carbon-coated $Ni_{0.5}Mg_{0.5}Fe_{1.7}Mn_{0.3}O_4$/C materials. Therefore, the XRD results confirm the formation of the $Ni_{0.5}Mg_{0.5}Fe_{1.7}Mn_{0.3}O_4$/C composite.

To conduct a more comprehensive examination of the structural characteristics, the X-ray diffraction (XRD) pattern of the synthesized $Ni_{0.5}Mg_{0.5}Fe_{1.7}Mn_{0.3}O_4$ spinel ferrite was subjected to refinement using the Rietveld method. Nevertheless, the process of structural refinement was conducted using the cubic structure and the $Fd\bar{3}m$ space group. Fig. 2(a) presents the Rietveld refinement plot for the synthesized $Ni_{0.5}Mg_{0.5}Fe_{1.7}Mn_{0.3}O_4$ spinel. The red circles represent the experimental X-ray diffraction (XRD) pattern, the black solid lines depict the theoretical XRD pattern, and the blue solid line corresponds to the difference curves. The vertical green bars indicate the positions of various Bragg reflections. Fig. 2(a) presented in this study demonstrates a strong correspondence between the observed X-ray diffraction (XRD) pattern and the calculated XRD pattern. This agreement provides evidence of the successful structural refinement achieved for the synthesized $Ni_{0.5}Mg_{0.5}Fe_{1.7}Mn_{0.3}O_4$ spinel ferrite. Furthermore, the evaluation of the quality of structural refinement was performed by considering several R-factors, such as the weighted profile factor (R_{wp}), profile factor (R_p), expected factor (R_{exp}), and Chi-squared value (χ^2). Table S1 (ESI†) summarizes the findings

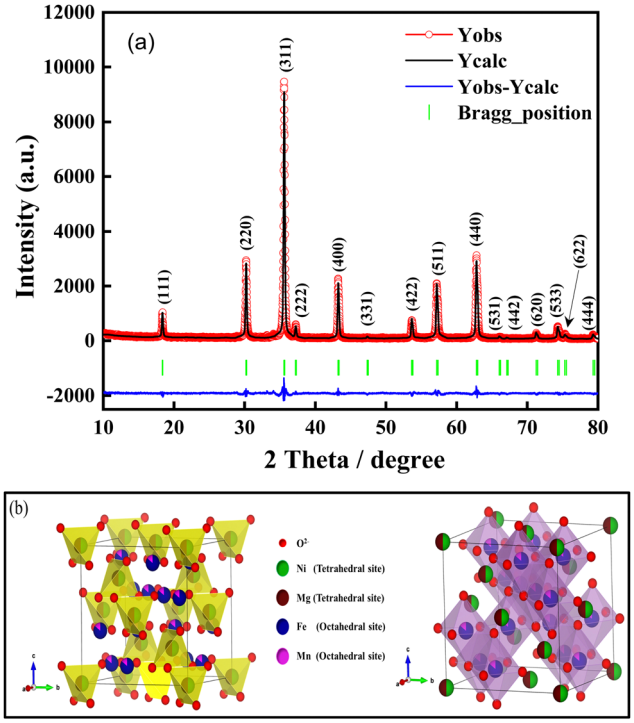

Fig. 2 (a) Rietveld analysis of the X-ray diffraction patterns for the synthesized $Ni_{0.5}Mg_{0.5}Fe_{1.7}Mn_{0.3}O_4$ material calcined at 800 °C. (b) Crystal structure of $Ni_{0.5}Mg_{0.5}Fe_{1.7}Mn_{0.3}O_4$ spinel with the cubic $Fd\bar{3}m$ structure, red balls represent the oxygen anions whereas the green-brown and blue-pink balls show the tetrahedral and octahedral sites, respectively.

from the powder X-ray diffraction analysis of the produced $Ni_{0.5}Mg_{0.5}Fe_{1.7}Mn_{0.3}O_4$ spinel oxide using Rietveld refinement. The results include structural parameters, Chi-squared factor (χ^2), and various reliability R-factors. Based on the obtained R-factors values, it can be concluded that the synthesized $Ni_{0.5}Mg_{0.5}Fe_{1.7}Mn_{0.3}O_4$ spinel oxide crystallizes in the cubic $Fd\bar{3}m$ structure, characterized by a lattice parameter of a = 8.36215 Å.

Fig. 2(b) illustrates the crystal structure of the $Ni_{0.5}Mg_{0.5}Fe_{1.7}Mn_{0.3}O_4$ sample, which exhibits cubic $Fd\bar{3}m$ symmetry. The analysis demonstrates that the synthesized material exhibits a crystal structure that is characterized by the connectivity of tetrahedra and octahedra sites, which are composed of oxygen anions. Based on the established framework, it becomes apparent that there are three distinct and easily discernible classifications of sites, denoted as 8a, 16d, and 32e sites. Notably, the 8a and 16d sites can be correlated with the tetrahedral and octahedral sites, respectively. The cations Ni^{2+} and Mg^{2+} are present in a ratio of 1/8 within the tetrahedral sites formed by the anions O^{2-}. Conversely, the cations Fe^{3+}/Mn^{3+} are situated in half of the octahedral sites formed by the anions O^{2-}. Furthermore, it should be noted that all the sites in the 32e structure are currently occupied by the O^{2-} anions. Hence, it is evident within the provided crystal structure that a substantial fraction of the tetrahedral sites (7/8) and half of the octahedral sites are vacant, thereby providing vacancies for the incorporation of lithium ions in the lacunae of the unit cell.

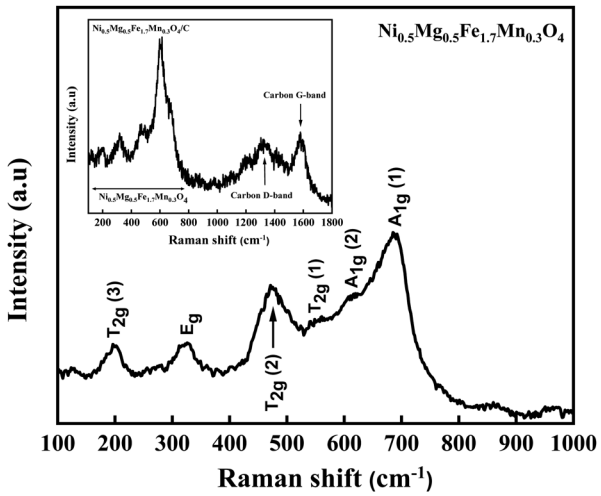

Fig. 3 Raman scattering curves collected at room temperature of the uncoated $Ni_{0.5}Mg_{0.5}Fe_{1.7}Mn_{0.3}O_4$ and carbon-coated $Ni_{0.5}Mg_{0.5}Fe_{1.7}Mn_{0.3}O_4$/C samples.

To further investigate the crystal structure of the synthesized $Ni_{0.5}Mg_{0.5}Fe_{1.7}Mn_{0.3}O_4$ material and to confirm the presence of a carbon layer in the $Ni_{0.5}Mg_{0.5}Fe_{1.7}Mn_{0.3}O_4$/C nanoparticles, Raman scattering spectroscopy was employed. Fig. 3 shows the Raman spectra of the uncoated $Ni_{0.5}Mg_{0.5}Fe_{1.7}Mn_{0.3}O_4$ and carbon-coated $Ni_{0.5}Mg_{0.5}Fe_{1.7}Mn_{0.3}O_4$/C materials. The Raman spectra of the coated material exhibit two distinct peaks at wavenumbers of approximately 1328.21 and 1582.06 cm^{-1}, which correspond to the typical D and G bands for carbon, respectively.[30,31] The D band is associated with the A_{1g} phonon of sp^3 carbon atoms at the edge and disordered carbon, while the G band is ascribed to the in-plane vibration of sp^2 carbon atoms in carbon atomic rings or long-chain carbon. The I_D/I_G ratio is a common evaluation value for carbon materials, indicating the degree of disorder and its association with electronic conductivity.[32,33] The calculated I_D/I_G value of 0.97 suggests a significant degree of disorder within the carbon structure of the as-prepared $Ni_{0.5}Mg_{0.5}Fe_{1.7}Mn_{0.3}O_4$/C composite, indicating amorphous carbon and agreeing with the XRD results.

The Raman spectra of the uncoated $Ni_{0.5}Mg_{0.5}Fe_{1.7}Mn_{0.3}O_4$ material exhibited six peaks between 100 and 700 cm^{-1}, which is also observed in the carbon-coated material.

It's pertinent to remember that, in the group theory analysis, the AB_2O_4-type spinels exhibiting cubic $Fd\bar{3}m$ symmetry are predicted to have five active Raman modes, which may be defined as A_{1g}, E_g, and $3T_{2g}$.[34] The Raman scattering spectra of the produced material, obtained at room temperature, are depicted in Fig. 3. The remarkable crystallinity of the $Ni_{0.5}Mg_{0.5}Fe_{1.7}Mn_{0.3}O_4$ sample is confirmed by the Raman spectra presented in Fig. 3. A total of six distinct Raman bands were detected at the respective wavenumbers of 189, 323, 473, 523, 650, and 691 cm^{-1}. The detected Raman bands, have distinct characteristics that align with the crystal structure of $MgFe_2O_4$, namely the cubic spinel configuration. This crystal structure is commonly associated with the $Fd\bar{3}m$ space group.[35]

Based on prior research, it has been shown that the Raman bands detected at a wavenumber of 189 cm^{-1} can be attributed to the T2g(3) mode, which signifies the vibrations of the localized lattice within the octahedral sub-lattice.[28] Nevertheless, it has been observed that two separate Raman bands have been found within the frequency range of 300–500 cm^{-1}. The bands seen in this study are associated with the Eg and T2g(2) vibrational modes. Specifically, these bands are allocated to the symmetric and asymmetric bending vibrations of the A/B–O tetrahedron.[23] In contrast, the three Raman peaks detected at elevated wavenumbers, namely at 523, 650, and 691 cm^{-1}, are ascribed to the asymmetric and symmetric stretching vibrations of oxygen atoms that are linked to metal ions situated within tetrahedral sites. The vibrational modes are designated as T2g(1) for asymmetric stretching vibrations and A1g for symmetric stretching vibrations, respectively. The Raman bands observed at a frequency greater than 600 cm^{-1} are attributed to the vibrational modes of the A-site. The A1g mode exhibits a distinct separation into two distinct modes at about 650 and 691 cm^{-1}, which can be attributed to the presence of various ions, specifically Mg^{2+} and Ni^{2+}, within the tetrahedral site.[36] This observation confirms the presence of a pure cubic spinel phase in the material that was synthesized.

The size and morphology of particles significantly impact the material's electrochemical performance. Creating active materials at the nanoscale is a highly efficient approach to enhancing electrode kinetics. Nanoparticles provide a larger contact area between the electrode and electrolyte, shorten the pathway for Li+ ion diffusion and electron movement, and increase the number of electrochemically active sites.[37]

The morphology of the as-prepared $Ni_{0.5}Mg_{0.5}Fe_{1.7}Mn_{0.3}O_4$ sample was investigated by SEM analysis, as illustrated in Fig. 4(a)–(c). The prepared material demonstrates the presence of spherical particles, with an average diameter of around 217 nm. Besides, EDS elemental mapping of $Ni_{0.5}Mg_{0.5}Fe_{1.7}Mn_{0.3}O_4$ is illustrated in Fig. 4(d)–(h) in which the signals corresponding to O, Mg, Ni, Fe, and Mn elements are detected with well-distributed elements and concentrated on the particles without obvious element segregation. Elemental analysis of the synthesized material was conducted using EDS spectroscopy.

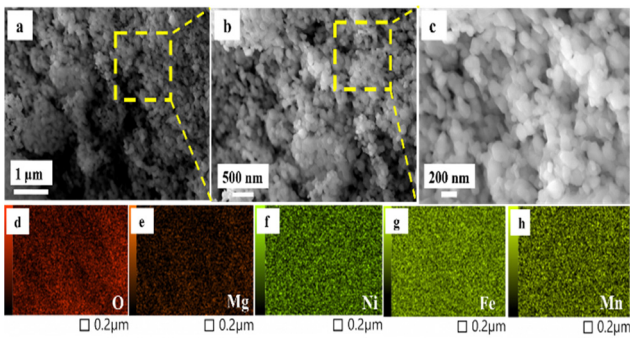

Fig. 4 (a)–(c) SEM images of $Ni_{0.5}Mg_{0.5}Fe_{1.7}Mn_{0.3}O_4$ material. (d)–(h) EDS mapping images of the O, Ni, Mg, Fe, and Mn elements for $Ni_{0.5}Mg_{0.5}Fe_{1.7}Mn_{0.3}O_4$ material.

The surface elemental composition of the $Ni_{0.5}Mg_{0.5}Fe_{1.7}Mn_{0.3}O_4$ material was determined using EDX analysis. Fig. S1, which can be found in the ESI,† provides evidence of the presence of nickel (Ni), magnesium (Mg), iron (Fe), manganese (Mn), and oxygen (O) in the as-synthesized sample, thereby confirming its purity.

TEM analysis was used to observe the inner microstructure of the uncoated and carbon-coated $Ni_{0.5}Mg_{0.5}Fe_{1.7}Mn_{0.3}O_4$ materials. The images are presented in Fig. 5 and Fig. S2 (ESI†). Fig. S2 (ESI†) shows that there is no carbon layer on the surface of the uncoated $Ni_{0.5}Mg_{0.5}Fe_{1.7}Mn_{0.3}O_4$ nanoparticles. However, Fig. 5(a)–(e) reveal amorphous carbon coating layers on the surface of the carbon-coated $Ni_{0.5}Mg_{0.5}Fe_{1.7}Mn_{0.3}O_4$/C nanoparticles. The homogeneity of various elements in the carbon-coated $Ni_{0.5}Mg_{0.5}Fe_{1.7}Mn_{0.3}O_4$/C powder was examined through high-angle annular dark-field scanning transmission electron microscopy (HAADF-STEM) along with corresponding elemental mapping technique. The images produced by HAADF-STEM and energy-dispersive spectroscopy (EDS) mapping of $Ni_{0.5}Mg_{0.5}Fe_{1.7}Mn_{0.3}O_4$/C, are presented in Fig. 5(f)–(l). These images reveal a consistent distribution of C, O, Ni, Mg, Fe, and Mn elements within the carbon-coated $Ni_{0.5}Mg_{0.5}Fe_{1.7}Mn_{0.3}O_4$/C nanoparticles.

The electrochemical performance of $Ni_{0.5}Mg_{0.5}Fe_{1.7}Mn_{0.3}O_4$ and $Ni_{0.5}Mg_{0.5}Fe_{1.7}Mn_{0.3}O_4$/C were evaluated by cyclic voltammetry and galvanostatic charge/discharge experiments at various current densities. These tests were conducted at room temperature, within a potential range ranging from 0.01 V to 3.0 V. Fig. 6 illustrates the cyclic voltammetry profile of the $Ni_{0.5}Mg_{0.5}Fe_{1.7}Mn_{0.3}O_4$ electrode within the voltage range of 0.01–3.0 V, with a scan rate of 1 mV s^{-1}. The initial cycle of the $Ni_{0.5}Mg_{0.5}Fe_{1.7}Mn_{0.3}O_4$ sample exhibits notable distinctions compared to subsequent cycles. This disparity can be attributed to the cathodic lithiation process during the first cycle, wherein two cathodic peaks are observed. A pronounced reduction peak is observed at a potential of 0.01 V (*versus* Li^+/Li), which is succeeded by a subsequent reduction peak occurring at 0.74 V (*versus* Li^+/Li). These peaks are likely a result of the incorporation of Li^+ ions into the $Ni_{0.5}Mg_{0.5}Fe_{1.7}Mn_{0.3}O_4$ material through a series of multistep reactions, these reactions could be assigned to the cations reduced to metallic status (Fe^{3+}/Fe^0, Mn^{3+}/Mn^0, and Ni^{2+}/Ni^0 without Mg^{2+} reduction to Mg^0 due to the high bond energy of MgO[38]) with the formation of SEI films and the generation of amorphous Li_2O (eqn (1)).[36,39] However, in this case, it can be observed that the cathodic peak at 0.01 V is indicative of the distinctive behavior associated with the insertion of Li^+ ions into the $Ni_{0.5}Mg_{0.5}Fe_{1.7}Mn_{0.3}O_4$ material.[40] The initial anodic peak observed at 1.8 V can be ascribed to the oxidation processes of iron (Fe) to ferric ions (Fe^{3+}), nickel (Ni) to nickel ions (Ni^{2+}), and manganese (Mn) to manganese ions (Mn^{2+}), facilitated by the creation of iron(III) oxide Fe_2O_3 (eqn (3)), MnO (eqn (4)), and NiO (eqn (2)) phases with the decomposition of the Li_2O phase.[7,25] Additionally, the pronounced cathodic peak recorded at a potential of 0.01 V (*vs.* Li^+/Li) during the initial cathodic peak could be ascribed to the formation of the solid–electrolyte interphase (SEI) layer, which arises from the decomposition of the electrolyte. This phenomenon is widely recognized for its significant contribution to the substantial reduction in capacity observed during the initial discharge cycle.[41] In the subsequent four CV cycles, they have similar cathodic and anodic peaks at 0.65 V and 1.9 V, respectively, The cathodic peaks for the subsequent four cycles could be linked to the reduction of NiO, Fe_2O_3, and MnO to Ni, Fe, and Mn, respectively. The following anodic process might be attributed to the oxidation of metallic nickel (Ni) to divalent ions (Ni^{2+}), metallic iron (Fe) to ferric ions (Fe^{3+}), and metallic manganese (Mn) to divalent ions (Mn^{2+}), indicating similar kinetics during the charge and discharge of the $Ni_{0.5}Mg_{0.5}Fe_{1.7}Mn_{0.3}O_4$ material.

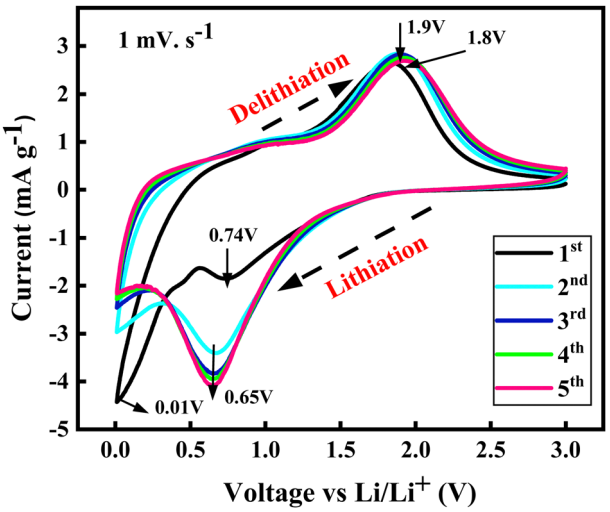

Fig. 6 Cyclic voltammetry profile in the voltage range of 0.01–3.0 V at a scan rate of 1 mV s^{-1} of the $Ni_{0.5}Mg_{0.5}Fe_{1.7}Mn_{0.3}O_4$ electrode.

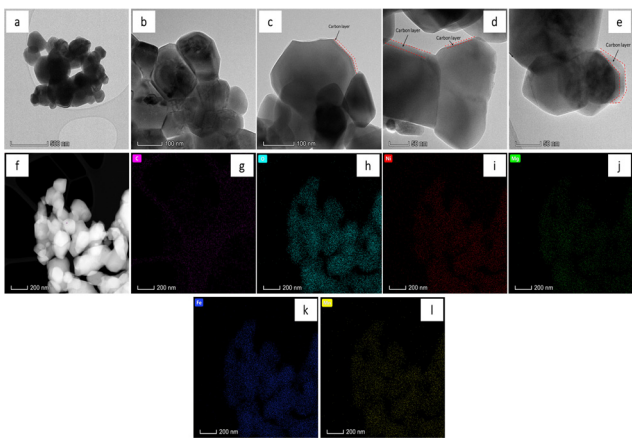

Fig. 5 (a)–(e) TEM images of carbon-coated $Ni_{0.5}Mg_{0.5}Fe_{1.7}Mn_{0.3}O_4$/C, (f) STEM image, and (g)–(l) corresponding elemental mapping images of the $Ni_{0.5}Mg_{0.5}Fe_{1.7}Mn_{0.3}O_4$/C sample.

Based on the literature,[25,26,42,43] and the analysis that has been previously discussed, the electrochemical reactions of the $Ni_{0.5}Mg_{0.5}Fe_{1.7}Mn_{0.3}O_4$ compound can be described as follows:

$$Ni_{0.5}Mg_{0.5}Fe_{1.7}Mn_{0.3}O_4 + 7.1Li^+ + 7.1e^- \rightarrow 0.5Ni + 0.5MgO + 1.7Fe + 0.3Mn + 3.55Li_2O \quad (1)$$

$$0.5Ni + 0.5Li_2O \leftrightarrow 0.5NiO + Li^+ + 1e^- \quad (2)$$

$$(1.7/2)Fe_2O_3 + 5.1Li^+ + 5.1e^- \leftrightarrow 1.7Fe + 2.55Li_2O \quad (3)$$

$$0.3MnO + 0.6Li^+ + 0.6e^- \leftrightarrow 0.3Mn + 0.3Li_2O \quad (4)$$

To improve the cycling stability of $Ni_{0.5}Mg_{0.5}Fe_{1.7}Mn_{0.3}O_4$ material, a carbon coating process was adopted. The carbon coating was demonstrated to improve the metal oxide's electrochemical stability during long-term cycling. The carbon prevents the metal oxide particle agglomeration and maintains the structure's stability. Additionally, it participates in reducing the volume change during discharge/charge processes and facilitates the Li^+ ion diffusion into the metal oxide's structure.[28,44] The charge–discharge profile of both uncoated and coated anode materials is depicted in Fig. 7(a) and (b). The data were obtained by conducting experiments within the voltage range of 0.01–3 V (*vs.* Li/Li^+) and at a current density of 100 mA g^{-1} for LIBs. The initial discharge and charge capacities for the uncoated and coated materials were determined to be 1275/874 and 1032/723 mA h g^{-1}, respectively, accompanied by initial coulombic efficiencies (ICE) of 68.54% and 70.06%, respectively. Consequently, the first coulombic efficiency of the $Ni_{0.5}Mg_{0.5}Fe_{1.7}Mn_{0.3}O_4$/C anode is slightly higher than that of the uncoated $Ni_{0.5}Mg_{0.5}Fe_{1.7}Mn_{0.3}O_4$ anode. This improvement may be attributed to the carbon layer, which protects the electrode materials from direct contact with the liquid electrolyte.[45] In addition, it is important to note that the initial capacity reduction during the first cycle is mainly due to the formation of a solid electrolyte interphase (SEI) layer on the electrode surface, accompanied by the generation of the inactive magnesium oxide phase (MgO).[46] In the 75th cycle, the charge capacities of uncoated and carbon-coated anode materials were 744 mA h g^{-1} and 806 mA h g^{-1} respectively. From the long-term cycling, the coated material shows an increase in capacity after 75 cycles compared to the uncoated material which shows a decrease in capacity, as indicated in Fig. 7(c). Moreover, the carbon-coated material displayed a capacity retention of approximately 89.7%, while reaching nearly 100% coulombic efficiency in the 75th cycle. The details of the electrochemical properties of these two electrodes are shown in Table S2 (ESI†). The excellent cycle stability of the $Ni_{0.5}Mg_{0.5}Fe_{1.7}Mn_{0.3}O_4$ material after carbon coating can be attributed to the stable solid electrolyte interphase (SEI) formed between the electrode and the electrolyte. Additionally, the improvement in the cycling stability of the coated material, compared to the uncoated sample, is a result of enhanced mechanical stability and stress resistance due to volume changes during the charge/discharge process. The coating limits the material's volume expansion by limiting its capacity; indeed, the anode did not reach its maximum capacity. Consequently, the volume change during lithiation is reduced, leading to improved stability.[47] As a result, both the electrochemical performance and cycling stability of the electrode are enhanced.

To better understand the advantages of carbon-coated $Ni_{0.5}Mg_{0.5}Fe_{1.7}Mn_{0.3}O_4$ nanoparticles in lithium-based energy storage, we compared the performance of uncoated $Ni_{0.5}Mg_{0.5}Fe_{1.7}Mn_{0.3}O_4$ and carbon-coated $Ni_{0.5}Mg_{0.5}Fe_{1.7}Mn_{0.3}O_4$/C rate

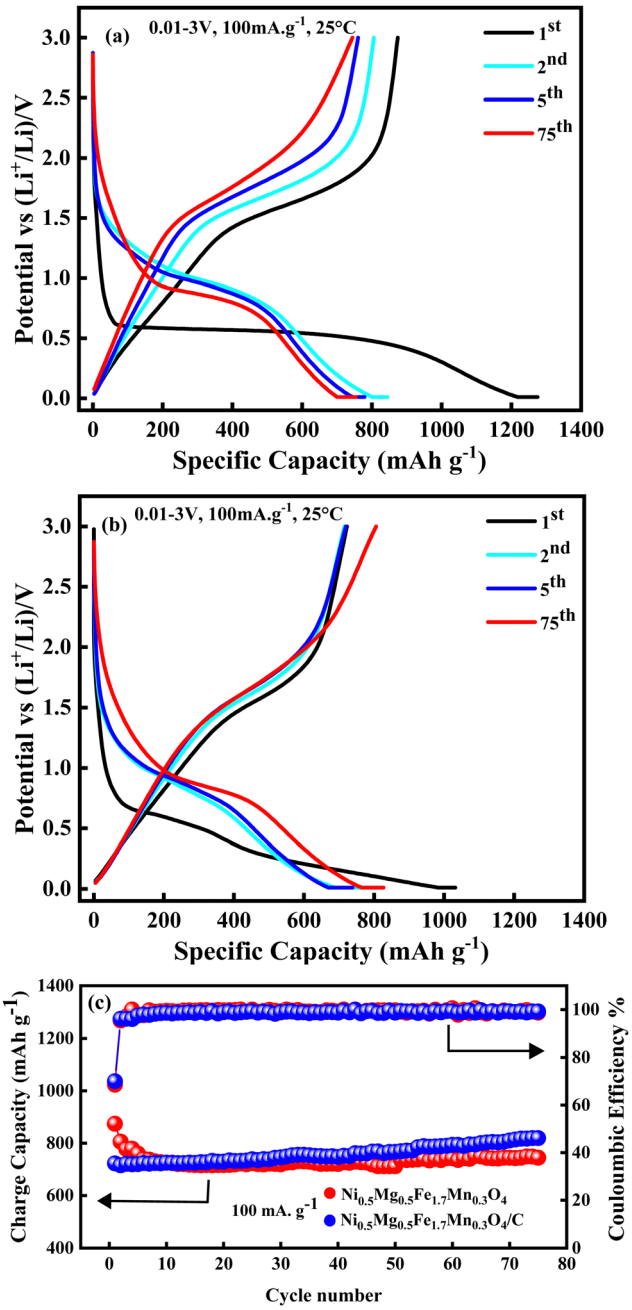

Fig. 7 Galvanostatic discharge/charge curves tested at a current density of 100 mA g^{-1} (100 mA g^{-1} = 0.125C) of (a) uncoated $Ni_{0.5}Mg_{0.5}Fe_{1.7}Mn_{0.3}O_4$ and (b) carbon-coated $Ni_{0.5}Mg_{0.5}Fe_{1.7}Mn_{0.3}O_4$/C electrodes. (c) Cycling performances of $Ni_{0.5}Mg_{0.5}Fe_{1.7}Mn_{0.3}O_4$ and $Ni_{0.5}Mg_{0.5}Fe_{1.7}Mn_{0.3}O_4$/C at a current density of 100 mA g^{-1} (100 mA g^{-1} = 0.125C).

capability in terms of Li^+ insertion/extraction (Fig. 8(a)). The two electrodes were cycled at different current rates of 0.03C, 0.06C, 0.125C, 0.25C, 0.625C, 1.25C and 2C, corresponding to 25, 50, 100, 200, 500, 1000 and 1600 mA g^{-1}. The coated electrode cell delivers average charge capacities of 720, 778, 760, 731, 690, 651, and 372 mA h g^{-1}. At the highest current density of 1600 mA g^{-1}, $Ni_{0.5}Mg_{0.5}Fe_{1.7}Mn_{0.3}O_4$/C delivers 372 mA h g^{-1} instead of the limited capacity of 192 mA h g^{-1}

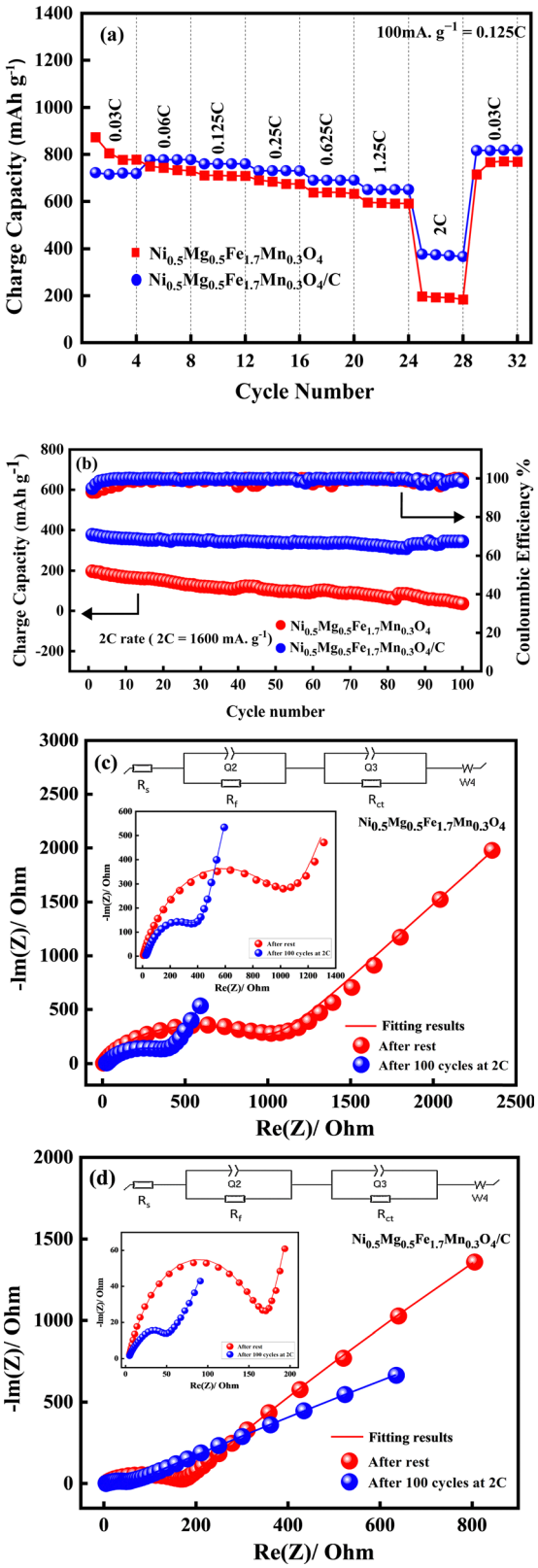

Fig. 8 The stability analysis of $Ni_{0.5}Mg_{0.5}Fe_{1.7}Mn_{0.3}O_4$ and $Ni_{0.5}Mg_{0.5}Fe_{1.7}Mn_{0.3}O_4$/C for comparison: (a) their rate capability from 0.03C to 2C (100 mA g^{-1} = 0.125C), (b) the cycling performance at 2C for 100 cycles, (c) and (d) their Nyquist plots before and after 100 cycles at 2C (100 mA g^{-1} = 0.125C).

for $Ni_{0.5}Mg_{0.5}Fe_{1.7}Mn_{0.3}O_4$. More importantly, when the current density was returned to 25 mA g^{-1}, a large irreversible capacity of 818 mA h g^{-1} was recovered, showing a strong tolerance to the rapid insertion/extraction of Li^+ ions. To further evaluate the long-term cycling performance at high current density, uncoated $Ni_{0.5}Mg_{0.5}Fe_{1.7}Mn_{0.3}O_4$, and carbon-coated $Ni_{0.5}Mg_{0.5}Fe_{1.7}Mn_{0.3}O_4$/C electrodes were charged and discharged for 100 cycles at 2C for comparison. As shown in Fig. 8(b), the uncoated material $Ni_{0.5}Mg_{0.5}Fe_{1.7}Mn_{0.3}O_4$ experienced an apparent capacity fading after 50 cycles and its capacity retention reached only 18.24% after 100 cycles, while the $Ni_{0.5}Mg_{0.5}Fe_{1.7}Mn_{0.3}O_4$/C still retained 91.17% of the initial discharge capacity after 100 cycles, reflecting the unstable structure of the uncoated $Ni_{0.5}Mg_{0.5}Fe_{1.7}Mn_{0.3}O_4$ and the stable structure of the carbon-coated $Ni_{0.5}Mg_{0.5}Fe_{1.7}Mn_{0.3}O_4$/C. The details of the electrochemical properties of these two electrodes are shown in Table S2 (ESI†).

To understand the carbon coating effect in more detail, electrochemical impedance spectroscopy (EIS) tests were performed before and after 100 cycles at a high current rate of 2C (100 mA g^{-1} = 0.125C). These tests were performed in the frequency range of 100 kHz to 0.01 Hz using cells with uncoated $Ni_{0.5}Mg_{0.5}Fe_{1.7}Mn_{0.3}O_4$ and carbon-coated $Ni_{0.5}Mg_{0.5}Fe_{1.7}Mn_{0.3}O_4$/C electrodes (Fig. 8(c) and (d)). From Fig. 8(c) and (d), the observed impedance spectra showed a semicircle in the high-frequency region, corresponding to the charge transfer resistance due to the transport of lithium ions across the electrode/electrolyte interface, and an inclined straight line in the low-frequency region, corresponding to the Warburg impedance due to the diffusion of Li^+ ions into the electrode materials.[48] Fig. 8(c) and (d) show the equivalent circuit model, consisting of the contact resistance (R_s), surface film resistance (R_f), charge transfer resistance (R_{ct}) and Warburg impedance (W_4); the fitting parameters are summarized in Table S3 (ESI†).[49] The R_{total} (where $R_{total} = R_s + R_f + R_{ct}$) can be closely monitored to explore the origin of the electrochemical properties of LiB cells in practice. A small R_{total} indicates improved cycling performance and rate capability of LiB. From the equivalent circuit model, the fitted R_{ct} parameter for cells before cycling are 18 646 and 10 237 Ω for uncoated $Ni_{0.5}Mg_{0.5}Fe_{1.7}Mn_{0.3}O_4$ and carbon-coated $Ni_{0.5}Mg_{0.5}Fe_{1.7}Mn_{0.3}O_4$/C electrodes, respectively. The lower R_{ct} value of the carbon-coated $Ni_{0.5}Mg_{0.5}Fe_{1.7}Mn_{0.3}O_4$/C electrode suggests a higher charge diffusion efficiency in this novel nanostructure.[50] Meanwhile, R_{ct} decreased to 2145 and 400 Ω after 100 cycles at a 2C rate for uncoated $Ni_{0.5}Mg_{0.5}Fe_{1.7}Mn_{0.3}O_4$ and carbon-coated $Ni_{0.5}Mg_{0.5}Fe_{1.7}Mn_{0.3}O_4$/C electrodes, respectively. It is observed that the R_{ct} values after 100 cycles were lower than those of the cell before cycling, indicating a lower charge transfer resistance, which suggests an improvement in electron transport during the repeated lithiation and delithiation processes. For R_{total}, the results indicate that the carbon-coated $Ni_{0.5}Mg_{0.5}Fe_{1.7}Mn_{0.3}O_4$/C electrode has a significantly lower total resistance after cycling compared to the uncoated $Ni_{0.5}Mg_{0.5}Fe_{1.7}Mn_{0.3}O_4$ and carbon-coated $Ni_{0.5}Mg_{0.5}Fe_{1.7}Mn_{0.3}O_4$/C electrodes before cycling, indicating improved stability and rate capability

performance. Thus, the EIS result shows that the $Ni_{0.5}Mg_{0.5}Fe_{1.7}Mn_{0.3}O_4$/C composite electrode has higher electrical conductivity compared to the uncoated $Ni_{0.5}Mg_{0.5}Fe_{1.7}Mn_{0.3}O_4$ material, resulting in stable and higher reversible capacity.

The $Ni_{0.5}Mg_{0.5}Fe_{1.7}Mn_{0.3}O_4$/C carbon-coated electrode exhibits excellent cycling performance and rate capability compared to the uncoated $Ni_{0.5}Mg_{0.5}Fe_{1.7}Mn_{0.3}O_4$ electrode, which is attributed to the protective carbon coating layer which protects the $Ni_{0.5}Mg_{0.5}Fe_{1.7}Mn_{0.3}O_4$ nanoparticles from direct contact with the electrolyte, thereby maintaining the structural integrity of the nanoparticles during the lithiation–delithiation process. Furthermore, the carbon layers not only mitigate the volume expansion of $Ni_{0.5}Mg_{0.5}Fe_{1.7}Mn_{0.3}O_4$ nanoparticles but also maintain stable electronic conductivity during the lithiation–delithiation process impedance text ref. 51.

To evaluate the performance of the carbon-coated $Ni_{0.5}Mg_{0.5}Fe_{1.7}Mn_{0.3}O_4$/C material in a complete battery system, a full cell was designed using an NMC811 cathode (Fig. 9(a) and (b)). The full cell's output voltage was 2.8 V at 0.125C current rate, within the voltage window of 1–4 V, matching the voltage difference between the NMC811 cathode and $Ni_{0.5}Mg_{0.5}Fe_{1.7}Mn_{0.3}O_4$/C anode. Furthermore, in Fig. 9(a), the charge/discharge cycles of the full cell at a 0.125C current rate are illustrated within the voltage range of 1–4 V. The full cell exhibited a capacity of 755 mA h g^{-1} with a coulombic efficiency of 65% during the first cycle, based on the mass of the $Ni_{0.5}Mg_{0.5}Fe_{1.7}Mn_{0.3}O_4$/C anode. Subsequently, after 4 cycles, the capacity decreased to 633 mA h g^{-1}, with an increase in the coulombic efficiency to 97%. The cycling performance of the full cell was investigated at 2C within the voltage window of 1–4 V (Fig. 9(b)). After 30 cycles, a capacity of 448 mA h g^{-1} was achieved with a capacity retention of 91% and a coulombic efficiency of 98%. The low capacity of the $Ni_{0.5}Mg_{0.5}Fe_{1.7}Mn_{0.3}O_4$/C electrode in the full cell is mainly due to its low first coulombic efficiency, which did not exceed 65%. The low first coulombic efficiency of the $Ni_{0.5}Mg_{0.5}Fe_{1.7}Mn_{0.3}O_4$/C anode may be attributed to various factors, such as the inadequate balance between the positive and negative electrodes, electrolyte decomposition during cycling, and other factors.

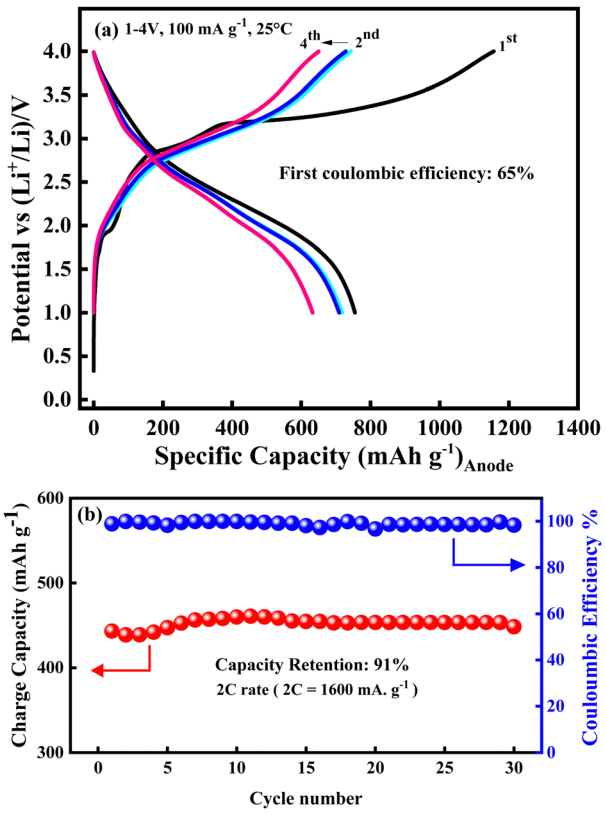

Fig. 9 (a) Charge/discharge cycle of the ($Ni_{0.5}Mg_{0.5}Fe_{1.7}Mn_{0.3}O_4$/C)/NMC811 full cell performed at a current density of 100 mA g^{-1} (100 mA g^{-1} = 0.125C) within the voltage range 1–4 V, (b) cycling performances at 2C charge/discharge rate.

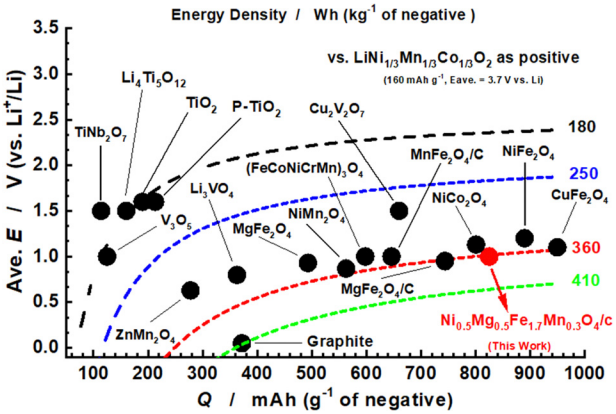

Fig. 10 A comparison of capacity, voltage, and energy density of anode materials for LIBs.

Fig. 10 shows the reversible capacity, the average potential, and the estimated energy density of anode materials for lithium full cells. In this study, we demonstrate that the $Ni_{0.5}Mg_{0.5}Fe_{1.7}Mn_{0.3}O_4$/C composite material displays a reversible capacity above 800 mA h g^{-1}. This value is notably 2–3 times greater than the reversible capacity observed in the graphite anode material,[35] and also shows a high specific capacity compared to the spinel $Li_4Ti_5O_{12}$,[52] TiO_2,[53] and Li_3VO_4,[54] anode materials. Furthermore, the energy density of spinel oxide $Ni_{0.5}Mg_{0.5}Fe_{1.7}Mn_{0.3}O_4$/C Li-ion cell is calculated to be 360 Wh kg^{-1} based on the capacity and the average potential of positive and negative electrodes with a relatively high operating voltage of 1.1 V *versus* Li/Li^+ compared to the traditional graphite.

4. Conclusion

In summary, $Ni_{0.5}Mg_{0.5}Fe_{1.7}Mn_{0.3}O_4$ spinel ferrite oxide nanoparticles were prepared using a simple and efficient sol–gel synthesis method and then coated with carbon. Analysis using X-ray diffraction and Raman spectroscopy confirmed that the synthesized materials have a single cubic spinel phase with the space group $Fd\bar{3}m$, and also confirmed the presence of an amorphous carbon layer on $Ni_{0.5}Mg_{0.5}Fe_{1.7}Mn_{0.3}O_4$/C nanoparticles. Scanning electron microscopy analysis highlighted the existence of spherical nanoparticles in the synthesized

substance, with a particle size of 217 nm. Further confirmation of the existence of the carbon layer was obtained through TEM analysis. The $Ni_{0.5}Mg_{0.5}Fe_{1.7}Mn_{0.3}O_4$ electrode was developed as an anode for lithium-ion batteries and demonstrated an initial specific capacity of over 874 mA h g^{-1}, as well as a capacity retention of approximately 85% after 75 cycles. Carbon-coated $Ni_{0.5}Mg_{0.5}Fe_{1.7}Mn_{0.3}O_4$/C nanoparticles exhibited excellent cycling stability as an anode for LIBs, with a capacity retention of approximately 89.7%. Furthermore, the carbon-coated $Ni_{0.5}Mg_{0.5}Fe_{1.7}Mn_{0.3}O_4$/C showed enhanced capacity, stability, and rate capability over extended cycling tests, underscoring the value of the carbon coating in improving the material's electrochemical performance. The combination of $Ni_{0.5}Mg_{0.5}Fe_{1.7}Mn_{0.3}O_4$/C material in a full-cell configuration with an NMC811 cathode demonstrated promising results, including high specific capacity, and stability after 30 cycles at 2C. These findings suggest that this material could serve as a promising candidate for next-generation anode materials in lithium-ion batteries.

Conflicts of interest

There are no conflicts to declare.

Acknowledgements

The authors would like to thank Office Chérifien des Phosphates (OCP S. A.), and Mohammed VI Polytechnic University for their invaluable financial support. Additionally, special thanks are due to the Argonne National Laboratory for providing the NMC811 electrodes utilized in this study.

References

1 D. Darbar, M. V. Reddy, S. Sundarrajan, R. Pattabiraman, S. Ramakrishna and B. V. R. Chowdari, Anodic electrochemical performances of $MgCo_2O_4$ synthesized by oxalate decomposition method and electrospinning technique for Li-ion battery application, *Mater. Res. Bull.*, 2016, **73**, 369–376.
2 S. Yuvaraj, R. K. Selvan and Y. S. Lee, *RSC Adv.*, 2016, **6**, 21448–21474.
3 M. T. Jeena, T. Bok, S. H. Kim, S. Perk, J. Y. Kim, S. Park and J. H. Ryu, A siloxane-incorporated copolymer as an in situ cross-linkable binder for high performance silicon anodes in Li-ion batteries, *Nanoscale*, 2016, **8**, 9245–9253.
4 F. Cheng, J. Liang, Z. Tao and J. Chen, Functional materials for rechargeable batteries, *Adv. Mater.*, 2011, **23**, 1695–1715.
5 F. Cheng, Z. Tao, J. Liang and J. Chen, Template-directed materials for rechargeable lithium-ion batteries, *Chem. Mater.*, 2008, **20**, 667–681.
6 J. Asenbauer, T. Eisenmann, M. Kuenzel, A. Kazzazi, Z. Chen and D. Bresser, *Sustainable Energy Fuels*, 2020, **4**, 5387–5416.
7 J. Liu, R. Wang, X. Zhong, K. Yan, Y. Li and Z. Xu, Li and Na storage behaviours of $MgFe_2O_4$ nanoparticles as anode materials for lithium ion and sodium ion batteries, *Int. J. Electrochem. Sci.*, 2019, **14**, 1725–1732.
8 Z. H. Li, T. P. Zhao, X. Y. Zhan, D. S. Gao, Q. Z. Xiao and G. T. Lei, High capacity three-dimensional ordered macroporous $CoFe_2O_4$ as anode material for lithium ion batteries, *Electrochim. Acta*, 2010, **55**, 4594–4598.
9 N. Schweikert, H. Hahn and S. Indris, Cycling behaviour of $Li/Li_4Ti_5O_{12}$ cells studied by electrochemical impedance spectroscopy, *Phys. Chem. Chem. Phys.*, 2011, **13**, 6234–6240.
10 J. Lim, E. Choi, V. Mathew, D. Kim, D. Ahn, J. Gim, S.-H. Kang and J. Kim, Enhanced High-Rate Performance of Li[sub 4]Ti[sub 5]O[sub 12] Nanoparticles for Rechargeable Li-Ion Batteries, *J. Electrochem. Soc.*, 2011, **158**, A275.
11 J. Wang, D. Kober, G. Shao, J. D. Epping, O. Görke, S. Li, A. Gurlo and M. F. Bekheet, Stable anodes for lithium-ion batteries based on tin-containing silicon oxycarbonitride ceramic nanocomposites, *Mater. Today Energy*, 2022, DOI: 10.1016/j.mtener.2022.100989.
12 G. N. Zhu, H. J. Liu, J. H. Zhuang, C. X. Wang, Y. G. Wang and Y. Y. Xia, Carbon-coated nano-sized $Li_4Ti_5O_{12}$ nanoporous micro-sphere as anode material for high-rate lithium-ion batteries, *Energy Environ. Sci.*, 2011, **4**, 4016–4022.
13 Y. Pan, Y. Zhang, X. Wei, C. Yuan, J. Yin, D. Cao and G. Wang, $MgFe_2O_4$ nanoparticles as anode materials for lithium-ion batteries, *Electrochim. Acta*, 2013, **109**, 89–94.
14 J. G. Kim, Y. Noh, Y. Kim, S. Lee and W. B. Kim, Formation of ordered macroporous $ZnFe_2O_4$ anode materials for highly reversible lithium storage, *Chem. Eng. J.*, 2019, **372**, 363–372.
15 S. Mitra, P. S. Veluri, A. Chakraborthy and R. K. Petla, Electrochemical Properties of Spinel Cobalt Ferrite Nanoparticles with Sodium Alginate as Interactive Binder, *ChemElectroChem*, 2014, **1**, 1068–1074.
16 M. Mujahid, R. Ullah Khan, M. Mumtaz, Mubasher, S. A. Soomro and S. Ullah, $NiFe_2O_4$ nanoparticles/MWCNTs nanohybrid as anode material for lithium-ion battery, *Ceram. Int.*, 2019, **45**, 8486–8493.
17 Z. Xing, Z. Ju, J. Yang, H. Xu and Y. Qian, One-step solid state reaction to selectively fabricate cubic and tetragonal $CuFe_2O_4$ anode material for high power lithium ion batteries, *Electrochim. Acta*, 2013, **102**, 51–57.
18 D. Narsimulu, B. N. Rao, M. Venkateswarlu, E. S. Srinadhu and N. Satyanarayana, Electrical and electrochemical studies of nanocrystalline mesoporous $MgFe_2O_4$ as anode material for lithium battery applications, *Ceram. Int.*, 2016, **42**, 16789–16797.
19 F. Wang, Y. Liu, Y. Zhao, Y. Wang, Z. Wang, W. Zhang and F. Ren, Facile synthesis of two-dimensional porous $MgCo_2O_4$ nanosheets as anode for lithium-ion batteries, *Appl. Sci.*, 2018, **8**(1), 22.
20 K. Kouchi, M. Tayoury, A. Chari, Z. Chchiyai, L. Hdidou, Y. Tamraoui, J. Alami, B. Manoun and M. Dahbi, in 2021 9th International Renewable and Sustainable Energy Conference (IRSEC), IEEE, 2021, pp. 1–5.
21 T. Li, X. Li, Z. Wang, H. Guo and Y. Li, A novel $NiCo_2O_4$ anode morphology for lithium-ion batteries, *J. Mater. Chem. A*, 2015, **3**, 11970–11975.

22 C. T. Cherian, J. Sundaramurthy, M. V. Reddy, P. Suresh Kumar, K. Mani, D. Pliszka, C. H. Sow, S. Ramakrishna and B. V. R. Chowdari, Morphologically robust $NiFe_2O_4$ nanofibers as high capacity Li-Ion battery anode material, *ACS Appl. Mater. Interfaces*, 2013, **5**, 9957–9963.

23 S. J. Rajoba, R. D. Kale, S. B. Kulkarni, V. G. Parale, R. Patil, H. Olin, H. H. Park, R. P. Dhavale and M. Phadatare, Synthesis and electrochemical performance of mesoporous $NiMn_2O_4$ nanoparticles as an anode for lithium-ion battery, *J. Compos. Sci.*, 2021, **5**(3), 69.

24 K. Cai, S. hua Luo, J. Cong, K. Li, S. xue Yan, P. qing Hou, Y. Song, Q. Wang, Y. Zhang, X. Liu, X. Lei, W. Mu and J. Gao, Sol–gel synthesis of nano block-like $ZnMn_2O_4$ using citric acid complexing agent and electrochemical performance as anode for lithium-ion batteries, *J. Alloys Compd.*, 2022, **909**, 164882.

25 Z. Chchiyai, L. Hdidou, M. Tayoury, A. Chari, Y. Tamraoui, J. Alami, M. Dahbi and B. Manoun, Synthesis and electrochemical properties of Mn-doped porous $Mg_{0.9}Zn_{0.1}$-$Fe_{2-x}Mn_xO4$ ($0 \leq x \leq 1.25$) spinel oxides as anode materials for lithium-ion batteries, *J. Alloys Compd.*, 2023, **935**, 167997.

26 N. Huo, Y. Yin, W. Liu, J. Zhang, Y. Ding, Q. Wang, Z. Shi and S. Yang, Facile synthesis of $MgFe_2O_4$/C composites as anode materials for lithium-ion batteries with excellent cycling and rate performance, *New J. Chem.*, 2016, **40**, 7068–7074.

27 L. Luo, D. Li, J. Zang, C. Chen, J. Zhu, H. Qiao, Y. Cai, K. Lu, X. Zhang and Q. Wei, Carbon-Coated Magnesium Ferrite Nanofibers for Lithium-Ion Battery Anodes with Enhanced Cycling Performance, *Energy Technol.*, 2017, **5**, 1364–1372.

28 Y. Yu, M. Li, Q. Li, J. Zhang, M. Sun, W. Qi and J. Li, Core–shell $MgFe_2O_4$@C nano-composites derived via thermal decomposition-reduction dual strategy for superior lithium storage, *J. Alloys Compd.*, 2020, **834**, 155207.

29 J. Mao, X. Hou, X. Wang, G. He, Z. Shao and S. Hu, Corncob-shaped $ZnFe_2O_4$/C nanostructures for improved anode rate and cycle performance in lithium-ion batteries, *RSC Adv.*, 2015, **5**, 31807–31814.

30 M. Zhang, X. Yang, X. Kan, X. Wang, L. Ma and M. Jia, Carbon-encapsulated $CoFe_2O_4$/graphene nanocomposite as high performance anode for lithium ion batteries, *Electrochim. Acta*, 2013, **112**, 727–734.

31 S. Li, B. Wang, J. Liu and M. Yu, In situ one-step synthesis of $CoFe_2O_4$/graphene nanocomposites as high-performance anode for lithium-ion batteries, *Electrochim. Acta*, 2014, **129**, 33–39.

32 H. Xia, D. Zhu, Y. Fu and X. Wang, $CoFe_2O_4$-graphene nanocomposite as a high-capacity anode material for lithium-ion batteries, *Electrochim. Acta*, 2012, **83**, 166–174.

33 L. Luo, D. Li, J. Zang, C. Chen, J. Zhu, H. Qiao, Y. Cai, K. Lu, X. Zhang and Q. Wei, Carbon-Coated Magnesium Ferrite Nanofibers for Lithium-Ion Battery Anodes with Enhanced Cycling Performance, *Energy Technol.*, 2017, **5**, 1364–1372.

34 W. B. White and B. A. DeAngelis, Interpretation of the vibrational spectra of spinels, *Spectrochim. Acta, Part A*, 1967, **23**, 985–995.

35 J. Chandradass, A. H. Jadhav, K. H. Kim and H. Kim, Influence of processing methodology on the structural and magnetic behavior of $MgFe_2O_4$ nanopowders, *J. Alloys Compd.*, 2012, **517**, 164–169.

36 C. Murugesan and G. Chandrasekaran, Structural and Magnetic Properties of $Mn_{1-x}Zn_xFe_2O_4$ Ferrite Nanoparticles, *J. Supercond. Novel Magn.*, 2016, **29**, 2887–2897.

37 J. Zhang, J. Qiao, K. Sun and Z. Wang, Balancing particle properties for practical lithium-ion batteries, *Particuology*, 2022, **61**, 18–29.

38 X. Wang, G. Zhai and H. Wang, Facile synthesis of $MgCo_2O_4$ nanowires as binder-free flexible anode materials for high-performance Li-ion batteries, *J. Nanopart. Res.*, 2015, **17**, 339.

39 M. Islam, G. Ali, M. G. Jeong, W. Choi, K. Y. Chung and H. G. Jung, Study on the Electrochemical Reaction Mechanism of $NiFe_2O_4$ as a High-Performance Anode for Li-Ion Batteries, *ACS Appl. Mater. Interfaces*, 2017, **9**, 14833–14843.

40 Y. Liu, N. Zhang, C. Yu, L. Jiao and J. Chen, $MnFe_2O_4$@C Nanofibers as High-Performance Anode for Sodium-Ion Batteries, *Nano Lett.*, 2016, **16**, 3321–3328.

41 C. Yue, Z. Liu, W. J. Chang, W. Il Park and T. Song, Hollow C nanobox: An efficient Ge anode supporting structure applied to high-performance Li ion batteries, *Electrochim. Acta*, 2018, **290**, 236–243.

42 G. Huang, F. Zhang, L. Zhang, X. Du, J. Wang and L. Wang, Hierarchical $NiFe_2O_4/Fe_2O_3$ nanotubes derived from metal organic frameworks for superior lithium ion battery anodes, *J. Mater. Chem. A*, 2014, **2**, 8048–8053.

43 J. G. Kim, Y. Noh, Y. Kim, S. Lee and W. B. Kim, Formation of ordered macroporous $ZnFe_2O_4$ anode materials for highly reversible lithium storage, *Chem. Eng. J.*, 2019, **372**, 363–372.

44 Y. Luo, C. Chen, L. Chen, M. Zhang and T. Wang, 3D reticular pomegranate-like $CoMn_2O_4$/C for ultrahigh rate lithium-ion storage with re-oxidation of manganese, *Electrochim. Acta*, 2017, **241**, 244–251.

45 L. Yao, X. Hou, S. Hu, J. Wang, M. Li, C. Su, M. O. Tade, Z. Shao and X. Liu, Green synthesis of mesoporous $ZnFe_2O_4$/C composite microspheres as superior anode materials for lithium-ion batteries, *J. Power Sources*, 2014, **258**, 305–313.

46 F. Luo, D. Ma, Y. Li, H. Mi, P. Zhang and S. Luo, Hollow Co_3S_4/C anchored on nitrogen-doped carbon nanofibers as a free-standing anode for high-performance Li-ion batteries, *Electrochim. Acta*, 2019, **299**, 173–181.

47 N. Huo, Y. Yin, W. Liu, J. Zhang, Y. Ding, Q. Wang, Z. Shi and S. Yang, Facile synthesis of $MgFe_2O_4$/C composites as anode materials for lithium-ion batteries with excellent cycling and rate performance, *New J. Chem.*, 2016, **40**, 7068–7074.

48 L. Luo, D. Li, J. Zang, C. Chen, J. Zhu, H. Qiao, Y. Cai, K. Lu, X. Zhang and Q. Wei, Carbon-Coated Magnesium Ferrite Nanofibers for Lithium-Ion Battery Anodes with Enhanced Cycling Performance, *Energy Technol.*, 2017, **5**, 1364–1372.

49 D. Narsimulu, B. N. Rao, N. Satyanarayana and E. S. Srinadhu, High Capacity Electrospun $MgFe_2O_4$–C

Composite Nanofibers as an Anode Material for Lithium Ion Batteries, *ChemistrySelect*, 2018, **3**, 8010–8017.
50 J. Wang, G. Yang, L. Wang, W. Yan and W. Wei, C@$CoFe_2O_4$ fiber-in-tube mesoporous nanostructure: Formation mechanism and high electrochemical performance as an anode for lithium-ion batteries, *J. Alloys Compd.*, 2017, **693**, 110–117.
51 L. Lin and Q. Pan, $ZnFe_2O_4$@C/graphene nanocomposite as excellent anode materials for lithium batteries, *J. Mater. Chem. A*, 2015, **3**, 1724–1729.
52 F. Liu, B. Bai, L. Cheng and C. Xu, Rapid synthesis of $Li_4Ti_5O_{12}$ as lithium-ion battery anode by reactive flash sintering, *J. Am. Ceram. Soc.*, 2022, **105**, 419–427.
53 N. El Halya, K. Elouardi, A. Chari, A. El Bouari, J. Alami and M. Dahbi, Chapter TiO_2 Based Nanomaterials and Their Application as Anode for Rechargeable Lithium-Ion Batteries, *Titanium Dioxide - Advances and Applications*, 2021.
54 E. Elmaataouy, A. Chari, M. Tayoury, J. Alami and M. Dahbi, in 2021 9th International Renewable and Sustainable Energy Conference (IRSEC), IEEE, 2021, pp. 1–4.